ACSNANO

www.acsnano.org

ARTICLE

# A Highly Selective Implantable Electrochemical Fiber Sensor for Real-Time Monitoring of Blood Homovanillic Acid

Kuangyi Zou, Qianming Li, Dan Li, Yiding Jiao, Lie Wang, Luhe Li, Jiacheng Wang, Yiran Li, Rui Gao, Fangyan Li, Er He, Tingting Ye, Wentao Tang, Jie Song, Jiang Lu, Xusong Li, Hanting Zhang, Xinyin Cao, and Ye Zhang*

Cite This: https://doi.org/10.1021/acsnano.3c11641

Read Online

ACCESS | Metrics & More | Article Recommendations | Supporting Information



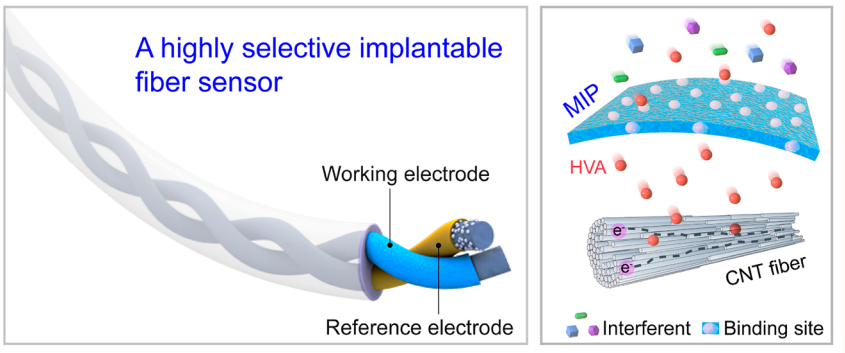


**ABSTRACT:** **Homovanillic acid (HVA) is a major dopamine metabolite, and blood HVA is considered as central nervous system (CNS) dopamine biomarker, which reflects the progression of dopamine-associated CNS diseases and the behavioral response to therapeutic drugs. However, facing blood various active substances interference, particularly structurally similar catecholamines and their metabolites, real-time and accurate monitoring of blood HVA remains a challenge. Herein, a highly selective implantable electrochemical fiber sensor based on a molecularly imprinted polymer is reported to accurately monitor HVA *in vivo*. The sensor exhibits high selectivity, with a response intensity to HVA 12.6 times greater than that of catecholamines and their metabolites, achieving 97.8% accuracy *in vivo*. The sensor injected into the rat caudal vein tracked the real-time changes of blood HVA, which paralleled the brain dopamine fluctuations and indicated the behavioral response to dopamine increase. This study provides a universal design strategy for improving the selectivity of implantable electrochemical sensors.**

**KEYWORDS:** *high selectivity, implantable fiber sensor, real-time monitoring, molecularly imprinted polymer, homovanillic acid*

## 1. INTRODUCTION

Homovanillic acid (HVA), a major metabolite of the pivotal central neurotransmitter dopamine, has the ability to cross the blood−brain barrier and enter the blood circulatory system, unlike dopamine.[1,2] Consequently, the fluctuation of blood HVA is closely related to dopamine activity in the central nervous system (CNS).[3−5] Clinically, CNS dopamine detection needs labor-intensive cerebrospinal fluid analysis or complex neurosurgery to implant the device which is prone to cause infection and permanent CNS function damage.[6,7] In contrast, blood samples are easy to collect and less invasive to implant, positioning the dynamic profile of blood HVA as a potent complement to existing methods for studying dopamine activity.[4,8] Furthermore, blood HVA is used as an indicator to assess the progression of schizophrenia and the effectiveness of related therapeutic drugs.[9,10] It has also been implicated in the pathogenesis of neurodegenerative diseases such as Parkinson's and Alzheimer's disease.[11−13] Therefore, real-time monitoring of blood HVA is of great significance for the study of central

Received: November 22, 2023
Revised: February 17, 2024
Accepted: February 23, 2024

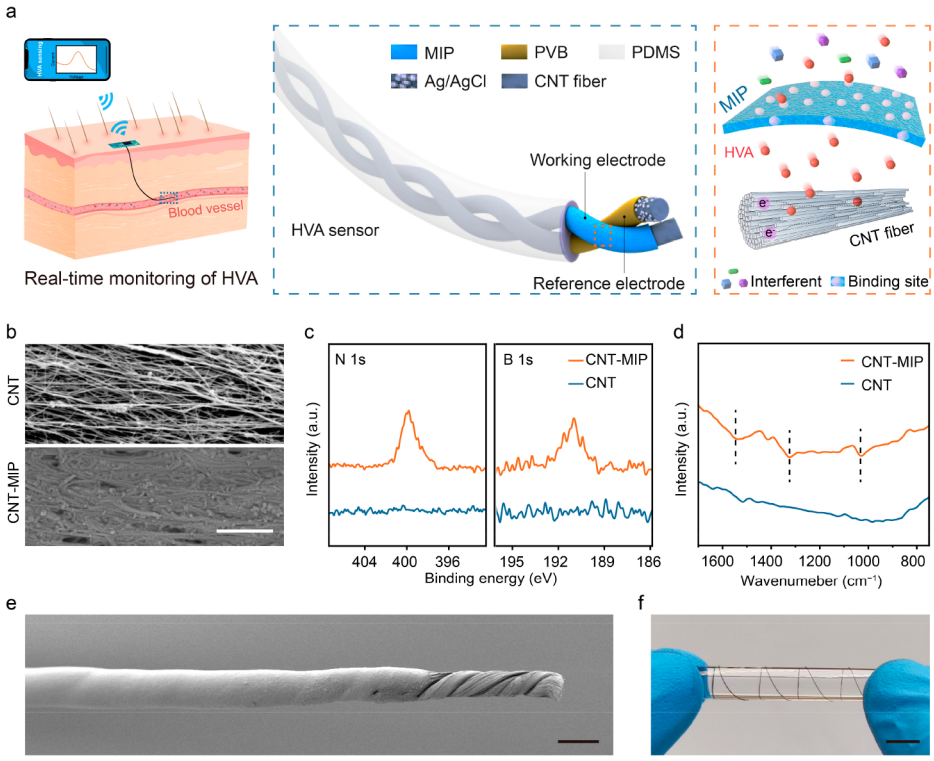


**Figure 1. Schematic illustration and structural characterization of a highly selective implantable electrochemical HVA fiber sensor. (a) Schematic illustration of an integrated system for wireless monitoring of HVA signals in blood using the implantable fiber sensor. (b) SEM images of the CNT and the CNT-MIP electrode. Scale bar, 1 $\mu$m. (c) High-resolution N 1s and B 1s XPS spectra of the CNT and the CNT-MIP electrode. (d) Fourier transform infrared spectroscopy of the CNT and the CNT-MIP electrode (from left to right 1547, 1324, and 1032 cm$^{-1}$, corresponding to the peaks of polypyrrole). (e) SEM image of the HVA sensor coated with an encapsulating layer of PDMS. Scale bar: 200 $\mu$m. (f) Optical image of the HVA fiber sensor wrapped around a glass rod. Scale bar: 5 mm.**

dopamine activity, disease pathogenesis, and drug efficacy evaluation.

However, real-time monitoring of HVA *in vivo* has not yet been achieved. The main challenge arises from the presence of numerous active substances in the blood, particularly catecholamines of the same type and their metabolites,[14] which have very similar molecular structures to HVA, even with a difference of only one functional group. It is difficult to distinguish them from HVA and to achieve accurate monitoring of blood HVA. Although clinical detection of blood HVA can currently be achieved by high-performance liquid chromatography or enzyme-linked immunosorbent assay (ELISA),[15−17] real-time monitoring remains challenging due to limitations in the frequency and quantity of blood sampling and the need to analyze collected samples in the laboratory for an extended period of time. Therefore, a tool for real-time monitoring of HVA *in vivo* remains an unmet need.

Herein, we have developed a highly selective implantable electrochemical fiber sensor for real-time monitoring of blood HVA. The high selectivity for HVA is accomplished by carefully designing the molecularly imprinted polymer (MIP), which allows only molecules that precisely match the recognition binding site to pass through, thus providing the sensor with *in vivo* selectivity for HVA. As a result, the sensor exhibited selectivity with a response to HVA 12.6 times greater than that to catecholamines and their metabolites, achieving an accuracy of 97.8% *in vivo*. In addition, the biocompatibility of the sensor was evaluated with no obvious thrombus, bioadhesion, or inflammation observed. After minimally invasive injection into the rat caudal vein, the sensor successfully monitored parallel changes in blood HVA concentration induced by CNS dopamine fluctuations and indicated excitatory behavior in rats in the meantime.

## 2. RESULTS AND DISCUSSION

**2.1. Fabrication and Characterization of the HVA Fiber Sensor.** Figure 1a shows the structure of the HVA fiber sensor, which consists of a working electrode and a reference electrode. Aligned carbon nanotube (CNT) fiber[18−20] was selected as the electrode material (Supporting Information (SI), Figure S1) due to its high flexibility with a bending stiffness of $1.96 \times 10^{-7}$ nN·m$^2$ and high conductivity of $10^4$ S·cm$^{-1}$. Then, a carefully designed MIP layer with binding sites of specific recognition was electrochemically deposited on the surface of the CNT fiber to produce the working electrode (SI, Figure S2). Here, pyrrole was chosen as the functional monomer because polypyrrole has been widely used *in vivo* and is considered safe.[21−23] The scanning electron microscope image of the working electrode clearly showed the aligned structure of the CNT fiber uniformly covered by a polymer film (Figure 1b). Meanwhile, characteristic elements N and B of the functional monomer pyrrole and the cross-linker 3-aminophenylboric acid appeared in the X-ray photoelectron spectroscopy, and characteristic peaks of polypyrrole were also found in the Fourier transform infrared spectroscopy (peaks at 1547, 1324, and 1032 cm$^{-1}$ corresponded to the stretching vibration of C=C in the polypyrrole ring, C−N stretching vibration, and N−H in-plane deformation),[24−26] indicating the


https://doi.org/10.1021/acsnano.3c11641
ACS Nano XXXX, XXX, XXX−XXX

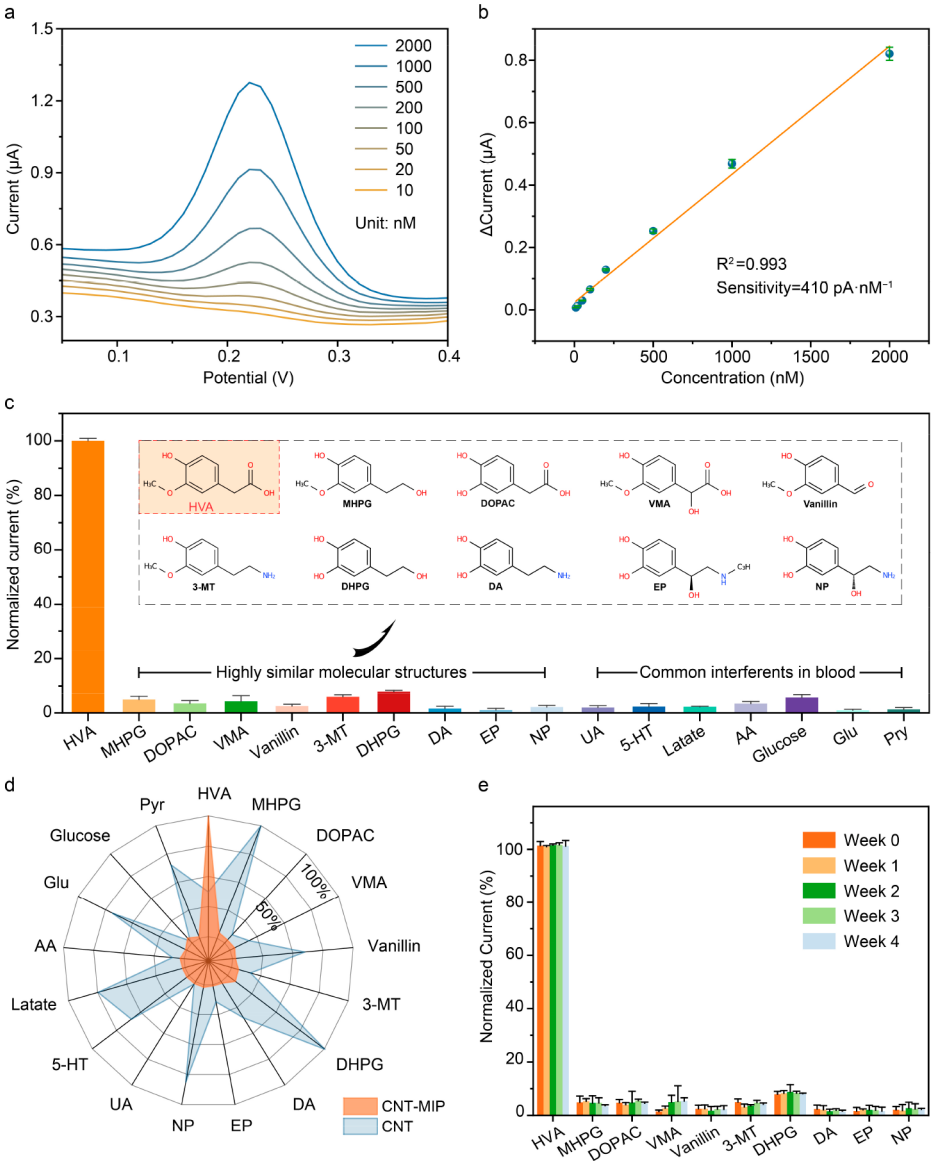


**Figure 2. Electrochemical sensing performance of the HVA fiber sensor *in vitro*.** (a) Response peak current of the sensor at different HVA concentrations performed by DPV (detection range: 0−2000 nM). (b) Linear relationship between response currents and HVA concentration (0−2000 nM). $n$ = 3. (c) Selectivity measurement of the HVA sensor: current response with the additions of HVA and a series of interfering substances at the same concentration (1 $\mu$M). Inset: Structural formula of the homovanillic acid molecule and its structurally similar molecule. MHPG, 3-methoxy-4-hydroxyphenylglycol; DOPAC, 3,4-dihydroxyphenylacetic acid; VMA, vanillylmandelic acid; 3-MT, 3-methoxytyramine; DHPG, 3,4-dihydroxyphenylethanol; DA, dopamine; EP, epinephrine; NP, norepinephrine; UA, uric acid; 5-HT, 5-hydroxytryptamine; AA, ascorbic acid; Glu, glutamic acid; Pyr, pyruvic acid. $n$ = 3. (d) Comparison of normalized current of the CNT and the CNT-MIP electrode toward HVA and interfering substances. The concentration of each substance is 1 $\mu$M. (e) Selectivity measurement from 0 to 4 weeks. Data are shown as the mean ± standard deviations. $n$ = 3. All tests were carried out in PBS electrolyte.

successful modification of MIP on the CNT fiber (Figure 1c,d). During the fabrication process, the ratio of template, cross-linker, and monomer was specifically set to 1:2:4 for the optimal sensitivity of HVA detection (SI, Figure S3). For the reference electrode, Ag/AgCl was deposited on the CNT fiber followed by polyvinyl butyral coating (SI, Figure S4). Finally, the HVA fiber sensor was fabricated by twisting the working and reference electrodes together to form a two-ply fiber configuration with polydimethylsiloxane (PDMS) as the encapsulation layer to ensure stable signals and prevent current crosstalk (Figure 1e, and SI, Figure S5). The HVA fiber sensor exhibited soft mechanical properties (Figure 1f) with a Young's modulus of 175 kPa (SI, Figure S6), which was in the same order of magnitude as skin and muscle tissue.[27,28]

**2.2. Electrochemical Sensing Performance of the HVA Fiber Sensor *in Vitro*.** To test the electrochemical sensing performance of the HVA fiber sensor, the response curves were first measured by differential pulse voltammetry (DPV) for HVA concentrations ranging from 10 nM to 2 $\mu$M (Figure 2a). A linear relationship between the peak current at +0.22 V and the HVA concentration (calibration curve) was obtained with a detection sensitivity of 410 pA·nM$^{-1}$ (Figure 2b). Moreover, chronoamperometry at +0.7 V was used to obtain a linear relationship ranging from 2 to 100 $\mu$M with a detection sensitivity of 83.7 pA·nM$^{-1}$ (SI, Figure S7), further


https://doi.org/10.1021/acsnano.3c11641
ACS Nano XXXX, XXX, XXX−XXX

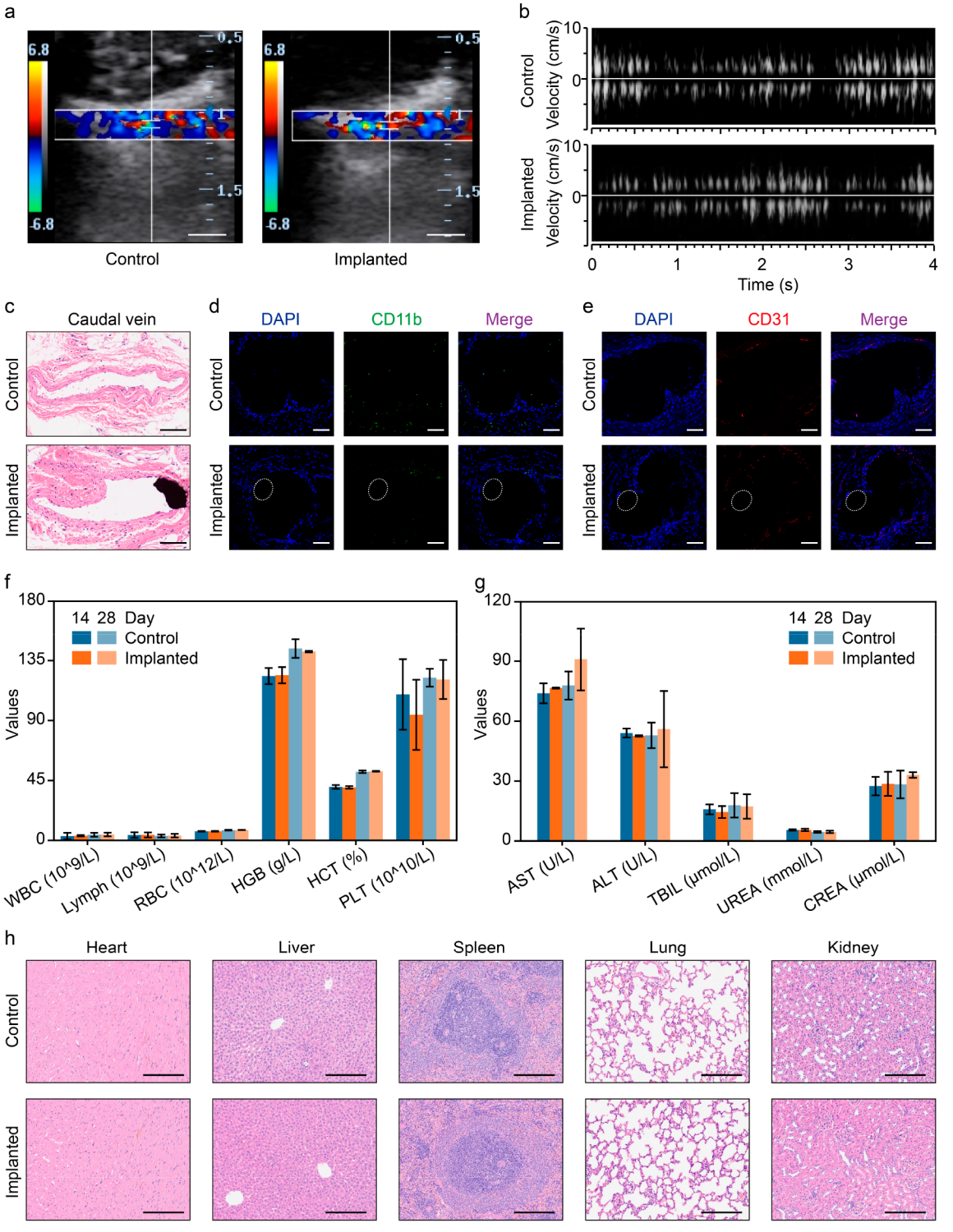


**Figure 3. Biocompatibility of the HVA fiber sensor.** (a) Representative blood flow color Doppler ultrasound images of the rat caudal vein of the control and implanted group after 28 days. Scale bar, 250 $\mu$m. (b) Blood flow velocity results of the control and implanted group after 28 days. (c) Representative H&E staining sections of the rat caudal vein from the control and implanted group after 28 days. Scale bar, 50 $\mu$m. (d,e) Visualization of inflammation and blood vessels by immune-staining with macrophage cell marker CD11b (green) and endothelial cell marker CD31 (red), in caudal vein with or without implantation for 28 days, respectively. DAPI, blue. Scale bar, 50 $\mu$m. (f) The changes of average counts of white blood cell (WBC), lymphocyte (Lymph), red blood cell (RBC), hemoglobin (HGB), hematocrit (HCT), and platelet (PLT) after implantation for 28 days. (g) The serum levels of aspartate transaminase (AST), alanine transaminase (ALT), total bilirubin (TBIL), urea (UREA), and creatinine (CREA) after implantation for 28 days. (h) Representative H&E staining sections of the major organs, including the heart, liver, spleen, lung, and kidney of rats with or without implanted HVA sensor for 28 days. Scale bar, 200 $\mu$m. Data are shown as the means $\pm$ standard deviations. $n$ = 6.



https://doi.org/10.1021/acsnano.3c11641
ACS Nano XXXX, XXX, XXX−XXX

extending the response range of the sensor and enabling it to detect the concentration of HVA in human blood under both normal and pathological conditions (48.3 nM to 6.9 $\mu$M).[29] For users of this sensor, the DPV method is performed first. If the concentration exceeds 3 $\mu$M (SI, Figure S8), then automatic switching to chronoamperometry will take place through a decision-making program for continuous monitoring. The detection limit of the sensor was calculated to be as low as 4.58 nM based on the calibration curve. This was attributed to the electrocatalytic effect of the CNT fiber on HVA (SI, Figure S9a), the peak current of which was at +0.17 V, slightly lower than the oxidation potential of the sensor due to the semiconductor nature of MIP, and the high electrochemical active surface area of the CNT fiber measured at 850 $cm^2 \cdot g^{-1}$ (SI, Figure S9b). The sensor also showed good repeatability with a standard deviation of only 3.5% between different samples (SI, Figure S10). Compared with the previously reported methods,[30−33] including fluorescence, high-performance liquid chromatography, and electrochemistry, the HVA fiber sensor demonstrated the lowest detection limit and widest response range at physiological pH (SI, Table S1), making it a promising candidate for real-time HVA monitoring.

Blood contains a large variety of bioactive molecules especially catecholamines of the same type and their metabolites, which have a very similar molecular structure to HVA, even differing by only one functional group.[14] Distinguishing them from HVA is essential for the accurate monitoring of HVA *in vivo*. The MIP membrane of the HVA sensor is highly selective for target molecules in interferents because it contains binding sites that are complementary to the target molecules.[34−37] The binding sites were further characterized by DPV and electrochemical impedance spectroscopy (SI, Figure S11). The subsequent decreased peak current height in DPV and increased resistance in Nyquist plots indicated that the MIP without a target molecule extracted impeded the charge transfer at the electrode−solution interface due to the increased surface coverage by the polymer. Extraction of the template molecule HVA led to the formation of selective binding sites in the polymer layer and increased the exposure of the CNT fibers to the sample matrix (details of the extraction process are provided in the Materials and Methods), resulting in a significant increase in peak current in DPV and a decrease in resistance in the Nyquist plot. In contrast, there was little sign of a pick-up in the peak current for the CNT-nonimprinted polymer after the extraction procedure (SI, Figure S12), further revealing the formation of binding sites in the MIP.

The selectivity of the HVA fiber sensor was then evaluated by adding catecholamines and their metabolites and common interfering agents in the blood into the analytical solution. Benefiting from the specific recognition ability of MIP, the response of the sensor to the target molecular was more than 12.6 times that of the interference response, showing excellent selectivity to HVA (Figure 2c). Additionally, the CNT-MIP electrode showed a specific response to HVA compared to the CNT electrode, which displayed a response to most of the interferents, further verifying the function of MIP as a recognition element (Figure 2d).

The stability of the HVA sensor was also evaluated by immersion in PBS solution at 37 °C for 4 weeks, during which the response current remained nearly unchanged with a fluctuation of less than 3.96% (SI, Figure S13). Moreover, as shown in Figure 2e, the result revealed that only HVA induced a large response current over 4 weeks, while the response to interferents was still negligible. These results showed that the stability of the sensor benefited from the essence of MIP as a cross-linked polymeric matrix. Finally, the binding sites of the HVA sensor can be regenerated repeatedly *in situ* without any washing step by applying a reverse potential for 30 s to repel bound HVA (SI, Figure S14), which is essential for continuous monitoring *in vivo* (SI, Figures S15 and S16).

In addition, the interference from physical activities was simulated to confirm the feasibility of the sensor for stable monitoring *in vivo*. After 1000 bending cycles, the impedance of the sensing fiber over a specific frequency remained stable with a fluctuation of 5.07% (SI, Figure S17), reflecting not only the stability of the internal structure of the electrode but also the stability of the electro−analyte interface. The response signals also showed no significant fluctuation during various simulated movements, including walking, shaking, sitting, jumping, and stooping (SI, Figure S18). These results demonstrated that the HVA sensor was electrochemically stable under physical activities, thus meeting the demand for stable monitoring *in vivo*. To minimize the size of the implanted sensors, a two-electrode system was used *in vivo* to monitor HVA (SI, Figure S19).

**2.3. Biocompatibility of the HVA Fiber Sensor.** To evaluate the biocompatibility of the HVA fiber sensor, cytotoxicity was first studied, and no significant differences in cell morphology, cell viability, and cell proliferation were observed compared to the control group after coculturing the HVA sensor with rat fibroblasts L929 and human umbilical vein endothelial cells (HUVEC) for 2 days (SI, Figure S20). Blood compatibility was then validated by plate adhesion, hemolysis, dynamic coagulation, and fibrin deposition tests.[38,39] The platelet adhesion behavior of the HVA sensor was not significantly different from that of the medical implantable titanium (Ti) wire (SI, Figure S21). The hemolysis rate of the sensor was only 0.57% (SI, Figure S22), and the dynamic coagulation time was consistent with that of the blank control group and Ti wire group (SI, Figure S23). The fibrin deposition and network formation were not significantly different between the sensor and Ti wire, suggesting that the two share a similar level of antifouling performance (SI, Figure S24). Due to the blood compatibility of the sensor, blood flow color Doppler ultrasound images and velocity results further validated that no thrombosis was formed on the 1st and 28th day of implantation compared to the control group (Figure 3a,b, and SI, Figure S25).

The inflammatory response of the caudal vein was evaluated by hematoxylin and eosin (H&E) and immunofluorescence staining after implantation for 28 days. H&E staining images showed that the tissue around the HVA sensor was similar to the control group, indicating no intimal hyperplasia and vascular plug formation (Figure 3c). Meanwhile, immunofluorescence-staining sections labeled with antibodies CD11b and CD31 showed that implantation of the sensor did not cause significant inflammatory cell infiltration or vascular proliferation (Figure 3d,e, and SI, Figure S26). After 14 and 28 days of implantation, there was no significant increase in the expression levels of serum proinflammatory cytokines (SI, Figure S27), indicating that the implantation of the sensor does not induce a noticeable immune response.

Chronic toxicity of the HVA fiber sensor implanted in the body was tested by blood analysis and characterization of


https://doi.org/10.1021/acsnano.3c11641
ACS Nano XXXX, XXX, XXX−XXX

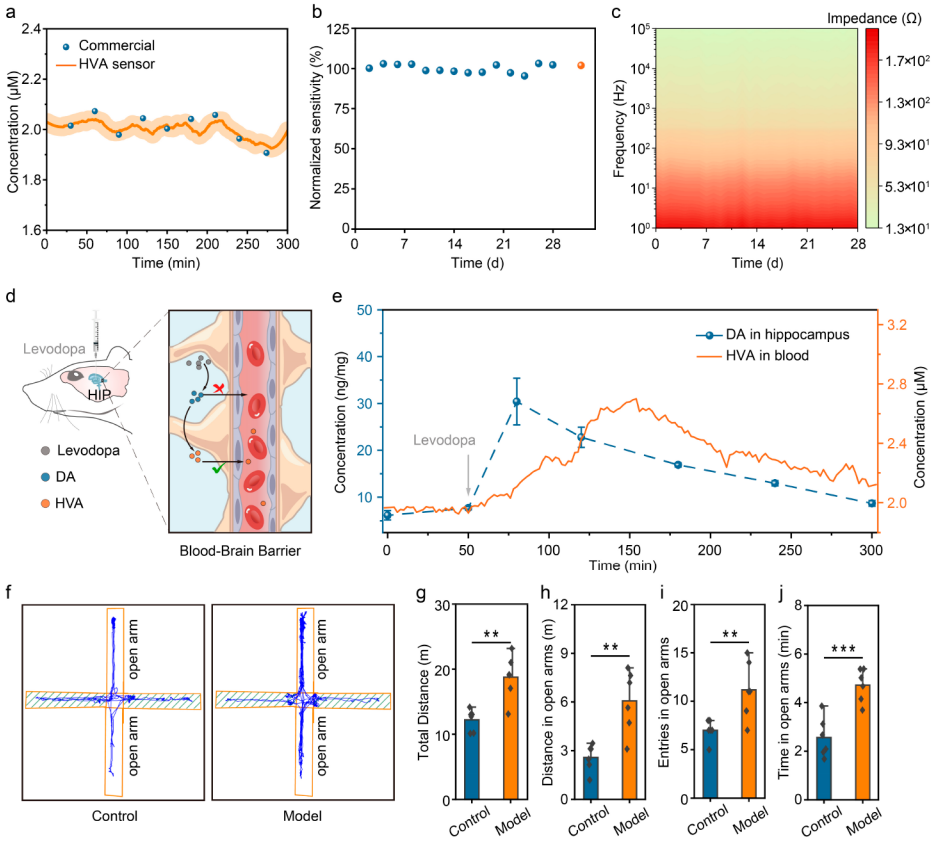


**Figure 4. Electrochemical sensing performance of the HVA fiber sensor *in vivo*. (a) Comparison between *ex situ* calibration data for HVA from collected blood samples and on body readings from the HVA fiber sensor. (b) The stable sensitivity of the HVA sensor *in vitro* for 28 days (blue dots). Another HVA fiber sensor was implanted in a rat caudal vein for 28 days and then tested *in vitro* (red dot). The red dot showed no obvious difference compared with the blue dots, indicating stable sensitivity *in vivo*. (c) The stable impedance magnitude of the HVA fiber sensor in the caudal vein of a rat during implantation for 28 days. (d) Schematic illustration of intracranial injection of levodopa and corresponding metabolic pathways. HIP: hippocampus. (e) Changes of dopamine concentration in the hippocampus (*ex situ* data from collected brain tissue) and HVA concentration in blood (on body reading from the integrated system using the HVA fiber sensor) after intracranial injection of levodopa. (f) Representative traces of the elevated plus maze (EPM) of the rats in the control and model group. $n$ = 6. Control, rats were injected intracranially and in the caudal vein with equal amounts of sterile PBS as in the model group; model, rats were injected intracranially with levodopa and implanted with HVA fiber sensors in the caudal vein. (g–j) EPM test statistics. The total distance during the EPM (g), distance in open arms (h), entries in open arms (i), and time spent in open arms (j). Data are shown as the means ± standard deviations. $n = 6$ * $P \leq 0.05$, ** $P \leq 0.01$, and ***$P \leq 0.001$.**

major organs. Then 28 days after implantation in rats, the average counts of white blood cells, lymphocytes, red blood cells, hemoglobin, and platelets and the level of hematocrit showed no significant difference between the implanted and control groups (Figure 3f). Besides, blood levels of enzymes and electrolytes, which served as indicators of organ-specific diseases, also fell within the confidence intervals of control values (Figure 3g). Moreover, the H&E staining tissue sections of the major organs, e.g., heart, liver, spleen, lung, and kidney, were analyzed and no noticeable pathological change was observed, indicating that the HVA sensor had no evident systemic side effects on the rats (Figure 3h). All of these results indicated that the HVA sensor demonstrated high blood compatibility and biosafety, thus meeting the demand for continuous monitoring *in vivo*.

**2.4. Electrochemical Sensing Performance of the HVA Fiber Sensor *in Vivo*.** The sensing performance *in vivo* of the HVA fiber sensor was tested after minimally invasive injection into the caudal vein of rats. The sensor was integrated with a flexible chip attached to the rat's back, which collected, processed, and wirelessly transmitted data to a Bluetooth-enabled mobile handset (SI, Figure S28). A freely behaving rat was tested, and the real-time electrochemical signal obtained from the mobile handset successfully reflected the normal fluctuations of blood HVA. As shown in Figure 4a, the data obtained from the sensor matched well with *ex situ* measurements of blood samples by a commercial ELISA kit with an accuracy of up to 97.8% (SI, Figure S29). Moreover, the real-time response of the sensor to changes in higher concentrations of HVA was studied by injecting a high concentration of HVA solution into fresh anticoagulant peripheral blood of rats, which also matched well with the results determined by the ELISA kit (SI, Figure S30). These results showed that the HVA sensor was both accurate and timely, serving as a continuous monitoring tool without the need for complex sampling procedures and cumbersome equipment.

The HVA sensor was retained in freely behaving rats for 4 weeks to validate its potential for long-term application *in vivo*. The sensitivity was found to be well maintained after chronic implantation *in vivo* for weeks compared to that of the *in vitro* test proceeding simultaneously (Figure 4b). The impedance


https://doi.org/10.1021/acsnano.3c11641
ACS Nano XXXX, XXX, XXX−XXX

magnitude of the sensor also remained stable throughout continuous monitoring (Figure 4c). Furthermore, the structure of the sensing fiber electrodes was well preserved after being implanted for 4 weeks, which accounted for the long-term electrochemical stability (SI, Figure S31). These results indicated a promising route with real-time monitoring of HVA in the blood over a continuous period of time.

Subsequently, the HVA sensor was applied to research on activity of dopamine in the CNS and presented as a proof of concept. Intracranial dopamine induction in rats was carried out by a target injection of levodopa (a medication commonly used to treat neurodegenerative diseases) into the hippocampus to prevent the influence of peripheral dopamine on experimental results (Figure 4d).[40,41] The levodopa was initially converted to dopamine, which caused the intracranial dopamine to rise afterward to the peak (30.41 ng/mg) after 30 min determined by *ex situ* measurements of brain tissue supernatant by commercial ELISA. Then, dopamine was gradually metabolized to HVA which entered the blood circulation through the blood−brain barrier. The concentration of HVA in the blood, monitored in real time by an HVA fiber sensor implanted in the rat caudal vein, increased gradually and peaked (2.7 $\mu$M) after 104 min, with a delay of 74 min compared to dopamine in the CNS (Figure 4e). Furthermore, along with the increase in HVA concentration in the blood, the rats exhibited excited behavior, which was verified by the elevated maze test (Figure 4f). As shown in Figure 4g−j, the moving trajectory, total distance, distance in the open arm, entries in the open arm, and time in the open arm of the model group presented significant differences compared to those of the control group, confirming the excitability of rats. The results validated the feasibility of assessing the trend of dopamine changes in the CNS and evaluating the behavioral response to therapeutic drugs through real-time monitoring of blood HVA by the sensor, avoiding the high trauma and risks caused by multiple craniotomy detection. Compared to the existing clinical dopamine detection techniques, the sensor demonstrated significant advantages in real-time continuous monitoring and ease of use (SI, Table S2).

## 3. CONCLUSIONS

In summary, we have developed an implantable electrochemical HVA fiber sensor by taking advantage of molecularly imprinted polymer to achieve highly selective (>12.6-fold), accurate (97.8%) and real-time monitoring of HVA *in vivo*. This work not only provides a promising tool for real-time monitoring of HVA concentration in blood, which is meaningful for the study of central dopamine activity with less invasiveness, disease diagnosis, and drug efficacy evaluation, but also demonstrates a universal strategy for improving the selectivity of implantable electrochemical sensors, thus broadening the monitoring range of biochemical substances *in vivo*.

## 4. MATERIALS AND METHODS

**4.1. Materials and Reagents.** Silver nitrate ($AgNO_3$, 99.8%), polyvinyl butyral (PVB, P105915), levodopa (99.0%), 3-aminophenylboric acid (APBA, 98.0%), homovanillic acid (HVA, >98.0%), ferric trichloride hexahydrate ($FeCl_3{\cdot}6H_2O$, ≥99.0%), 3,4-dihydroxyphenylacetic acid (98.0%), 3-methoxy-4-hydroxymandelic acid (98.0%), 4-(2-aminoethyl)-2-methoxyphenol (≥95.0%), ascorbic acid (>99.0%), uric acid (99.0%), norepinephrine (98.0%), 4-hydroxy-3-methoxyphenylethanol (≥95.0%), ethanol (≥99.9%), pyruvic acid (96.0%), and glutamic acid (≥99.9%) were purchased from Shanghai Aladdin Biochemical Technology Co., Ltd. L-Lactate (98.0%), D-(+)-glucose (99.5%) and Nafion (5 wt % in a mixture of lower aliphatic alcohols and water) were acquired from Sigma-Aldrich. Phosphate buffer saline (PBS, pH = 7.4), potassium chloride (KCl, ≥99.5%), sodium bisulfite ($NaHSO_3$, AR), sodium chloride (NaCl, 99.5%), hydrogen chloride (HCl, AR), and potassium ferricyanide ($K_3Fe(CN)_6$, ≥99.9%) were obtained from Sinopharm Chemical Reagent Co., Ltd. Sodium thiosulfate ($Na_2S_2O_3$, 99.0%), pyrrole (99.0%), epinephrine (99.0%), 3,4-dihydroxyphenylethanol (98.0%), dopamine (98.0%), and potassium ferrocyanide ($K_4Fe(CN)_6$, 99.0%) were purchased from Shanghai Macklin Biochemical Co., Ltd. Polydimethylsiloxane (PDMS, including a SYLGARD 184 silicone elastomer base and its curing agent) was purchased from Dow Corning. Serotonin (≥99.9%), vanillin (99.5%), rat homovanillic acid ELISA kit, bovine serum albumin (BSA, 20 mg·mL$^{-1}$), Triton X-100 (99.0%), human fibrinogen (FBG), and goat antihuman fibrinogen/fluorescein isothiocyanate (FITC) were purchased from Nantong Feiyu Biological Technology Co., Ltd. Rat dopamine (DA) ELISA kit was obtained from Meimian Industrial Co., Ltd. (Jiangsu, China). Sodium tetraphenylborate buffer (pH = 9.18) was obtained from Leici (Shanghai, China). Whole pig blood was purchased from Shanghai Yuanye Bio-Technology Co., Ltd. Human umbilical vein endothelial cells (HUM-iCell-e005) and mouse fibroblast cells L929 (iCell-m026) were purchased from iCell Bioscience Inc. (Shanghai, P. R. China). Dulbecco's Modified Eagle's Medium (DMEM), fetal bovine serum (FBS), and trypsin-EDTA were purchased from Gibco (Shanghai, P. R. China). Enhanced Cell Counting Kit-8 and Calcein/PI Live/Dead Viability/Cytotoxicity Assay Kit were purchased from Beyotime Biotechnology Technology Co., Ltd.

**4.2. Preparation of HVA Working Fiber Electrode.** The CNT fiber was immersed into the polymerization solution, which was prepared by dissolving 2.5 mM HVA, 6.25 mM APBA, and 18.25 mM pyrrole into phosphate-buffered saline (pH = 7.4), and the imprinted polymer was electrochemically synthesized on the CNT fiber electrode with CV deposition (0−1 V for three cycles, 50 mV·s$^{-1}$). Subsequently, the target molecules (HVA) were extracted by soaking the electrode into a sodium tetraphenylboride buffer (pH = 9.18) with arbitrary constant potential step wave at 0.2 V for 60 s, 0.7 V for 60 s, 1.2 V for 60 s, 0.7 V for 60 s, and 0.2 V for 60 s for 10 cycles, and this process took 50 min. The HVA working fiber electrode was acquired after being rinsed with deionized water and dried at room temperature. For nonimprinted polymer (NIP), the electrode was prepared following the same procedure as MIP except that no template molecule HVA was added to the polymerization solution.

**4.3. Preparation of Ag/AgCl Reference Fiber Electrode.** The CNT fiber was coated with Ag nanoparticles in a solution containing 0.25 M $AgNO_3$, 0.75 M $Na_2S_2O_3$, and 0.5 M $NaHSO_3$ by multicurrent electrodeposition at −0.01 mA for 150 s, −0.02 mA for 50 s, −0.05 mA for 50 s, −0.08 mA for 50 s, and −0.1 mA for 350 s. Subsequently, a chlorination process was implemented by dipping the fiber into a 0.1 M $FeCl_3$ solution for 30 s. Finally, the Ag/AgCl reference fiber electrode was obtained by drop-coating 4 $\mu$L of PVB solution, which was prepared by dissolving PVB (79.1 mg) and NaCl (50 mg) into 1 mL of ethanol.

**4.4. Fabrication of HVA Fiber Sensor.** The HVA working fiber electrode and Ag/AgCl reference fiber electrode were coated with PDMS (PDMS was prepared with the silicone elastomer base and its cross-linking agent at a weight ratio of 10:1) and solidified at 80 °C for 1 h as the insulating layer. Then, the sensing fiber and the reference fiber were arranged in parallel. Subsequently, one end was fixed by a rotating motor shaft and the other was fixed by adhesive tape, with the motor operating at a speed of 200 rad·min$^{-1}$ to form a helical structure. Finally, the PDMS was coated again to fix the helical structure, and the HVA fiber sensor was acquired.

**4.5. Characterization of the HVA Fiber Sensor.** The morphology of the HVA fiber sensor was characterized by scanning electron microscopy (SEM, Hitachi FE-SEM S-4800). Gold nanoparticles were deposited at 110 mA for 30 s on the surface of the


https://doi.org/10.1021/acsnano.3c11641
ACS Nano XXXX, XXX, XXX−XXX

sensor by a sputter coater (Leica, EM ACE600). X-ray photoelectron spectroscopy (XPS) was carried out with a K-Alpha X-ray photoelectron spectrometer (ThermoFisher). The spectra were calibrated using the C 1s peak at 284.8 eV. Fourier-transform infrared spectroscopy (FTIR) was carried out using a Nicolet IS50 spectrometer (ThermoFisher). Tensile tests were carried out with a HY-0580 tensile tester (Hengyi) at a rate of 10 mm·min$^{-1}$.

**4.6. Electrochemical Performance Testing *in Vitro*.** The electrochemical performance of the sensor was carried out with a three-electrode system. HVA sensing fiber electrode, Ag/AgCl electrode, and Pt electrode were used as working, reference, and counter electrodes, respectively. Cyclic voltammetry (CV) was carried out for the study of the catalyst effect of the CNT fiber, with the CV condition as follows: range, 0−1 V; scanning rate, 20 mV·s$^{-1}$. Differential pulse voltammetry (DPV) analysis was performed for sensor characterization in PBS (pH = 7.4), with the DPV conditions as follows: range, 0−1 V; incremental potential, 0.01 V; pulse amplitude, 0.05 V; pulse width, 0.05 s; pulse period, 0.5 s. Open circuit potential−electrochemical impedance spectroscopy (vs frequency) was performed for the study of the electrochemical stability of the HVA sensor, with a frequency range of 1−100000 Hz, alternating current amplitude, 10 mV. All the electrochemical measurements were carried out using a CorrTest CS350 electrochemical workstation and repeated at least three times. The repetitions for every described experiment were different sensors, each tested once. Gas protection was maintained by using Ar gas throughout the test. The limit of detection (LOD) was calculated by using the following formula:

$$\mathrm{LOD} = \frac{3 \times S_b}{k}$$

Where $k$ was the slope of the calibration curve and $S_b$ was the standard deviation of the intercept of the calibration curve.

**4.7. Implantation of the HVA Fiber Sensor and Wireless Continuous Monitoring.** The HVA fiber sensor was threaded into a syringe prefilled with sterilized normal saline with the sensing site kept in the needle and the other parts left in the syringe body. Then, the SD rats were given with 1% isoflurane at an airflow rate of 1000 cc·min$^{-1}$ for anesthesia induction and 2.5% isoflurane at an airflow rate of 800 cc·min$^{-1}$ for anesthesia. After the rat' tail was cleaned with iodophor and 75% (v/v) alcohol, the sensor was implanted into the caudal vein through intravenous injection. The end of the sensor was connected to a commercial flexible (E104-BT02-V4.2) fixed on the back of the rat by 3 M tape, which prevented scratching of the rats. The electrical signals detected by the sensor were converted to concentration signals, which were wirelessly transmitted to a mobile phone via Bluetooth and displayed on the screen in real time.

**4.8. Electrochemical Performance Testing and Calibration *in Vivo*.** First, the rats were anesthetised with amobarbital sodium solutions (1%, 40 mg·kg$^{-1}$), and the HVA fiber sensor was injected into the caudal vein. Next, the electrochemical test *in vivo* was performed with a two-electrode system. Meanwhile, the blood samples were collected and measured by a commercial enzyme-linked immunosorbent assay (ELISA), which was conducted to evaluate the accuracy of the sensor by comparing it with the data acquired continuously *in vivo*. The accuracy is defined as follows:

$$\mathrm{accuracy}(\%) = \frac{|C_{in} - C_{ex}|}{C_{ex}} \times 100\%$$

$C_{in}$ was the data acquired from the sensor, and the $C_{ex}$ was the data measured by the commercial ELISA.

**4.9. Enzyme-Linked Immunosorbent Assay.** The blood was collected from the caudal vein of each rat and was centrifuged (3000 rpm, 4 °C, 10 min) to acquire plasma for the HVA test at different time points. The 15% hippocampi were isolated and blotted dry and then weighed and prepared as a 5% tissue homogenate in ice-cold 0.9% saline solution. After centrifugation (1500*g*, 4 °C, 10 min), the supernatant was obtained for the dopamine test at different time points. The concentrations of dopamine and HVA were measured by rat dopamine and HVA ELISA kits according to the manufacturer's instructions. The absorbance at an optical density of 450 nm was determined by a Synergy 2 microplate reader.

**4.10. Blood Flow Color Doppler Ultrasound Imaging.** Blood flow color Doppler ultrasound imaging (Mindray, Vetus 8) was used to evaluate the blood flow velocity and the presence of thrombosis. Rats were anesthetized with (1.5−2.5) % isoflurane and kept supine on a heated platform during imaging. The tail was cleaned with an iodophor and 75% (v/v) alcohol.

**4.11. Techniques for Intracranial Dopamine Induction in Rats.** First, a 50 mg portion of levodopa was dissolved in 10 μL of 0.1 M HCl and 10 mL of glucose solution (50 mg/mL) was added to obtain levodopa injection. Then, the rats were anesthetized with 2% isoflurane mixed with oxygen and fixed on a stereotactic brain frame. After marking a scalp incision, the connective tissue and periosteum were carefully removed using a scalpel to expose the brain' skull. A 0.3 mm diameter hole was drilled at the skull, and 10 μL of sterilized levodopa was slowly injected into the designated brain regions with the help of a micro pusher on the brain stereotaxic instrument (hippocampus: AP, −4.16 mm; DV, 7 mm; ML, 5 mm; Paxinos−Watson map).

**3.12. The Elevated Plus Maze Test.** The rats were released from the central platform individually and allowed to explore the maze freely for 5 min with a camera positioned overhead. The total distance and the time spent, the distance traveled, and the number of entries in the open arms were recorded.

## ASSOCIATED CONTENT

### Supporting Information

The Supporting Information is available free of charge at https://pubs.acs.org/doi/10.1021/acsnano.3c11641.

Preparation methods of carbon nanotube fiber, biosafety tests including cell live/dead viability test, hemotoxylin and eosin (H&E) and immunohistochemical staining, hematology and blood chemistry, hemolysis test, platelet adhesion test, dynamic coagulation test, and fibrin deposition assay; photograph of CNT fiber, SEM images of Ag/AgCl reference fiber electrode and HVA fiber sensor, schematic illustration of the fabrication process of MIP modification, MIPs electrochemical characterization, the effect of the sensor on the proliferation of L929 and HUVEC cells, platelet adsorption, dynamic clotting time, the blood flow color Doppler ultrasound images, proinflammatory cytokines expression levels in serum, the integrated system for wirelessly monitoring blood HVA; performance comparison of different methods for the detection of HVA and comparison of different methods for clinical monitoring of dopamine (PDF)

## AUTHOR INFORMATION

### Corresponding Author

**Ye Zhang** − *National Laboratory of Solid State Microstructures, Jiangsu Key Laboratory of Artificial Functional Materials, Chemistry and Biomedicine Innovation Center, Collaborative Innovation Center of Advanced Microstructures, College of Engineering and Applied Sciences, Nanjing University, Nanjing 210023, China;* orcid.org/0000-0002-7376-6547; Email: yezhang@nju.edu.cn

### Authors

**Kuangyi Zou** − *National Laboratory of Solid State Microstructures, Jiangsu Key Laboratory of Artificial Functional Materials, Chemistry and Biomedicine Innovation Center, Collaborative Innovation Center of Advanced*



https://doi.org/10.1021/acsnano.3c11641
ACS Nano XXXX, XXX, XXX−XXX

*Microstructures, College of Engineering and Applied Sciences, Nanjing University, Nanjing 210023, China*

**Qianming Li** − *National Laboratory of Solid State Microstructures, Jiangsu Key Laboratory of Artificial Functional Materials, Chemistry and Biomedicine Innovation Center, Collaborative Innovation Center of Advanced Microstructures, College of Engineering and Applied Sciences, Nanjing University, Nanjing 210023, China*

**Dan Li** − *Department of Immunology, School of Medicine and Holistic Integrative Medicine, Nanjing University of Chinese Medicine, Nanjing 210023, China*

**Yiding Jiao** − *National Laboratory of Solid State Microstructures, Jiangsu Key Laboratory of Artificial Functional Materials, Chemistry and Biomedicine Innovation Center, Collaborative Innovation Center of Advanced Microstructures, College of Engineering and Applied Sciences, Nanjing University, Nanjing 210023, China;* orcid.org/0000-0002-3536-7510

**Lie Wang** − *National Laboratory of Solid State Microstructures, Jiangsu Key Laboratory of Artificial Functional Materials, Chemistry and Biomedicine Innovation Center, Collaborative Innovation Center of Advanced Microstructures, College of Engineering and Applied Sciences, Nanjing University, Nanjing 210023, China*

**Luhe Li** − *National Laboratory of Solid State Microstructures, Jiangsu Key Laboratory of Artificial Functional Materials, Chemistry and Biomedicine Innovation Center, Collaborative Innovation Center of Advanced Microstructures, College of Engineering and Applied Sciences, Nanjing University, Nanjing 210023, China*

**Jiacheng Wang** − *National Laboratory of Solid State Microstructures, Jiangsu Key Laboratory of Artificial Functional Materials, Chemistry and Biomedicine Innovation Center, Collaborative Innovation Center of Advanced Microstructures, College of Engineering and Applied Sciences, Nanjing University, Nanjing 210023, China*

**Yiran Li** − *National Laboratory of Solid State Microstructures, Jiangsu Key Laboratory of Artificial Functional Materials, Chemistry and Biomedicine Innovation Center, Collaborative Innovation Center of Advanced Microstructures, College of Engineering and Applied Sciences, Nanjing University, Nanjing 210023, China*

**Rui Gao** − *National Laboratory of Solid State Microstructures, Jiangsu Key Laboratory of Artificial Functional Materials, Chemistry and Biomedicine Innovation Center, Collaborative Innovation Center of Advanced Microstructures, College of Engineering and Applied Sciences, Nanjing University, Nanjing 210023, China*

**Fangyan Li** − *National Laboratory of Solid State Microstructures, Jiangsu Key Laboratory of Artificial Functional Materials, Chemistry and Biomedicine Innovation Center, Collaborative Innovation Center of Advanced Microstructures, College of Engineering and Applied Sciences, Nanjing University, Nanjing 210023, China*

**Er He** − *National Laboratory of Solid State Microstructures, Jiangsu Key Laboratory of Artificial Functional Materials, Chemistry and Biomedicine Innovation Center, Collaborative Innovation Center of Advanced Microstructures, College of Engineering and Applied Sciences, Nanjing University, Nanjing 210023, China*

**Tingting Ye** − *National Laboratory of Solid State Microstructures, Jiangsu Key Laboratory of Artificial Functional Materials, Chemistry and Biomedicine Innovation Center, Collaborative Innovation Center of Advanced Microstructures, College of Engineering and Applied Sciences, Nanjing University, Nanjing 210023, China*

**Wentao Tang** − *Department of Immunology, School of Medicine and Holistic Integrative Medicine, Nanjing University of Chinese Medicine, Nanjing 210023, China*

**Jie Song** − *National Laboratory of Solid State Microstructures, Jiangsu Key Laboratory of Artificial Functional Materials, Chemistry and Biomedicine Innovation Center, Collaborative Innovation Center of Advanced Microstructures, College of Engineering and Applied Sciences, Nanjing University, Nanjing 210023, China*

**Jiang Lu** − *National Laboratory of Solid State Microstructures, Jiangsu Key Laboratory of Artificial Functional Materials, Chemistry and Biomedicine Innovation Center, Collaborative Innovation Center of Advanced Microstructures, College of Engineering and Applied Sciences, Nanjing University, Nanjing 210023, China*

**Xusong Li** − *National Laboratory of Solid State Microstructures, Jiangsu Key Laboratory of Artificial Functional Materials, Chemistry and Biomedicine Innovation Center, Collaborative Innovation Center of Advanced Microstructures, College of Engineering and Applied Sciences, Nanjing University, Nanjing 210023, China*

**Hanting Zhang** − *National Laboratory of Solid State Microstructures, Jiangsu Key Laboratory of Artificial Functional Materials, Chemistry and Biomedicine Innovation Center, Collaborative Innovation Center of Advanced Microstructures, College of Engineering and Applied Sciences, Nanjing University, Nanjing 210023, China*

**Xinyin Cao** − *National Laboratory of Solid State Microstructures, Jiangsu Key Laboratory of Artificial Functional Materials, Chemistry and Biomedicine Innovation Center, Collaborative Innovation Center of Advanced Microstructures, College of Engineering and Applied Sciences, Nanjing University, Nanjing 210023, China*

Complete contact information is available at: https://pubs.acs.org/10.1021/acsnano.3c11641

### Author Contributions

Kuangyi Zou, Qianming Li, and Dan Li contributed equally to this work. All authors discussed the results and assisted in the final of the manuscript.

### Notes

The authors declare no competing financial interest.

## ACKNOWLEDGMENTS

All animal studies were approved by the Animal Ethical and Welfare Committee of Nanjing University (approval no.: IACUC-2309009, Nanjing, China). This work was financially supported by the National Natural Science Foundation of China (22175086, 22005137, 82201992), the Natural Science Foundation of Jiangsu Province (BK20200321, BK20210681), the Program for Innovative Talents and Entrepreneurs in Jiangsu (JSSCTD202138), and Natural Science Foundation of Nanjing University of Chinese Medicine (XPT82201992).

## REFERENCES

(1) Obermeier, B.; Daneman, R.; Ransohoff, R. M. Development, Maintenance and Disruption of the Blood-Brain Barrier. *Nat. Med.* **2013**, *19*, 1584−1596.

(2) Mori, S.; Takanaga, H.; Ohtsuki, S.; Deguchi, T.; Kang, Y. S.; Hosoya, K.; Terasaki, T. Rat Organic Anion Transporter 3 ($Roat_3$) Is Responsible for Brain-To-Blood Efflux of Homovanillic Acid at the Abluminal Membrane of Brain Capillary Endothelial Cells. *J. Cereb Blood Flow Metab* **2003**, *23*, 432−440.
(3) Pickar, D.; Labarca, R.; Linnoila, M.; Roy, A.; Hommer, D.; Everett, D.; Paul, S. M. Neuroleptic-Induced Decrease in Plasma Homovanillic Acid and Antipsychotic Activity in Schizophrenic Patients. *Science* **1984**, *225*, 954−957.
(4) Castro-Fornieles, J.; Deulofeu, R.; Martinez-Mallen, E.; Baeza, I.; Fernandez, L.; Lazaro, L.; Toro, J.; Vila, M.; Bernardo, M. Plasma Homovanillic Acid in Adolescents with Bulimia Nervosa. *Psychiatry Res.* **2009**, *170*, 241−244.
(5) Zhang, Z. J.; Peet, M.; Ramchand, C. N.; Shah, S.; Reynolds, G. P. Plasma Homovanillic Acid in Untreated Schizophrenia−Relationship with Symptomatology and Sex. *J. Psychiatr Res.* **2001**, *35*, 23−28.
(6) Li, J.; Liu, Y.; Yuan, L.; Zhang, B.; Bishop, E. S.; Wang, K.; Tang, J.; Zheng, Y. Q.; Xu, W.; Niu, S.; Beker, L.; Li, T. L.; Chen, G.; Diyaolu, M.; Thomas, A. L.; Mottini, V.; Tok, J. B.; Dunn, J. C. Y.; Cui, B.; Pasca, S. P.; Cui, Y.; Habtezion, A.; Chen, X.; Bao, Z. A Tissue-Like Neurotransmitter Sensor for the Brain and Gut. *Nature* **2022**, *606*, 94−101.
(7) Stuart, T.; Jeang, W. J.; Slivicki, R. A.; Brown, B. J.; Burton, A.; Brings, V. E.; Alarcon-Segovia, L. C.; Agyare, P.; Ruiz, S.; Tyree, A.; Pruitt, L.; Madhvapathy, S.; Niemiec, M.; Zhuang, J.; Krishnan, S.; Copits, B. A.; Rogers, J. A.; Gereau, R. W. t.; Samineni, V. K.; Bandodkar, A. J.; Gutruf, P. Wireless, Battery-Free Implants for Electrochemical Catecholamine Sensing and Optogenetic Stimulation. *ACS Nano* **2023**, *17*, 561−574.
(8) Baeza, I.; Castro-Fornieles, J.; Deulofeu, R.; de la Serna, E.; Goti, J.; Salva, J.; Bernardo, M. Plasma Homovanillic Acid Differences in Clinical Subgroups of First Episode Schizophrenic Patients. *Psychiatry Res.* **2009**, *168*, 110−118.
(9) McCutcheon, R. A.; Krystal, J. H.; Howes, O. D. Dopamine and Glutamate in Schizophrenia: Biology, Symptoms and Treatment. *World Psychiatry* **2020**, *19*, 15−33.
(10) Kegeles, L. S.; Abi-Dargham, A.; Frankle, W. G.; Gil, R.; Cooper, T. B.; Slifstein, M.; Hwang, D. R.; Huang, Y.; Haber, S. N.; Laruelle, M. Increased Synaptic Dopamine Function in Associative Regions of the Striatum in Schizophrenia. *Arch Gen Psychiatry* **2010**, *67*, 231−239.
(11) Baiguera, C.; Alghisi, M.; Pinna, A.; Bellucci, A.; De Luca, M. A.; Frau, L.; Morelli, M.; Ingrassia, R.; Benarese, M.; Porrini, V.; Pellitteri, M.; Bertini, G.; Fabene, P. F.; Sigala, S.; Spillantini, M. G.; Liou, H. C.; Spano, P. F.; Pizzi, M. Late-Onset Parkinsonism in Nfkappab/C-Rel-Deficient Mice. *Brain* **2012**, *135*, 2750−2765.
(12) Zhou, J.; Li, J.; Papaneri, A. B.; Kobzar, N. P.; Cui, G. Dopamine Neuron Challenge Test for Early Detection of Parkinson's Disease. *NPJ. Parkinsons Dis* **2021**, *7*, 116.
(13) Parnetti, L.; Gaetani, L.; Eusebi, P.; Paciotti, S.; Hansson, O.; El-Agnaf, O.; Mollenhauer, B.; Blennow, K.; Calabresi, P. CSF and Blood Biomarkers for Parkinson's Disease. *Lancet Neurol* **2019**, *18*, 573−586.
(14) Goldstein, D. S.; Eisenhofer, G.; Kopin, I. J. Sources and Significance of Plasma Levels of Catechols and Their Metabolites in Humans. *J. Pharmacol Exp Ther* **2003**, *305*, 800−811.
(15) Towers, A. E.; Oelschlager, M.; Patel, J.; Lawson, M.; McCusker, R.; Freund, G. Acute Calorie Restriction Modifies Cognition and Anxiety-Like Behavior in Mice by Regulating IL-1$\beta$ Priming and Activation Within the Brain. *Brain Behav Immun* **2015**, *49*, e17−18.
(16) Fowler, A. J.; Hebron, M.; Missner, A. A.; Wang, R.; Gao, X.; Kurd-Misto, B. T.; Liu, X.; Moussa, C. E. Multikinase Abl/DDR/Src Inhibition Produces Optimal Effects for Tyrosine Kinase Inhibition in Neurodegeneration. *Drugs R D* **2019**, *19*, 149−166.
(17) Pagan, F. L.; Hebron, M. L.; Wilmarth, B.; Torres-Yaghi, Y.; Lawler, A.; Mundel, E. E.; Yusuf, N.; Starr, N. J.; Anjum, M.; Arellano, J.; Howard, H. H.; Shi, W.; Mulki, S.; Kurd-Misto, T.; Matar, S.; Liu, X.; Ahn, J.; Moussa, C. Nilotinib Effects on Safety, Tolerability, and Potential Biomarkers in Parkinson Disease: A Phase 2 Randomized Clinical Trial. *JAMA Neurol* **2020**, *77*, 309−317.
(18) Wang, L.; Xie, S.; Wang, Z.; Liu, F.; Yang, Y.; Tang, C.; Wu, X.; Liu, P.; Li, Y.; Saiyin, H.; Zheng, S.; Sun, X.; Xu, F.; Yu, H.; Peng, H. Functionalized Helical Fibre Bundles of Carbon Nanotubes As Electrochemical Sensors for Long-Term In Vivo Monitoring of Multiple Disease Biomarkers. *Nat. Biomed Eng.* **2020**, *4*, 159−171.
(19) Xu, X.; Xie, S.; Zhang, Y.; Peng, H. The Rise of Fiber Electronics. *Angew. Chem., Int. Ed. Engl.* **2019**, *58*, 13643−13653.
(20) Li, Q.; Li, D.; Lu, J.; Zou, K.; Wang, L.; Jiao, Y.; Wang, M.; Gao, R.; Song, J.; Li, Y.; et al. Interface-Stabilized Fiber Sensor for Real-Time Monitoring of Amniotic Fluid During Pregnancy. *Adv. Mater.* **2024**, *35*, No. 2307726.
(21) Wang, F.; Li, Q.; Park, J. O.; Zheng, S.; Choi, E. Ultralow Voltage High-Performance Bioartificial Muscles Based on Ionically Crosslinked Polypyrrole-Coated Functional Carboxylated Bacterial Cellulose for Soft Robots. *Adv. Funct. Mater.* **2021**, *31*, No. 2007749.
(22) Wang, X.; Ma, Y.; Sheng, X.; Wang, Y.; Xu, H. Ultrathin Polypyrrole Nanosheets via Space-Confined Synthesis for Efficient Photothermal Therapy in the Second Near-Infrared Window. *Nano Lett.* **2018**, *18*, 2217−2225.
(23) Zha, Z.; Yue, X.; Ren, Q.; Dai, Z. Uniform Polypyrrole Nanoparticles with High Photothermal Conversion Efficiency for Photothermal Ablation of Cancer Cells. *Adv. Mater.* **2013**, *25*, 777−82.
(24) Li, L.; Li, D.; Wang, Y.; Ye, T.; He, E.; Jiao, Y.; Wang, L.; Li, F.; Li, Y.; Ding, J.; Liu, K.; Ren, J.; Li, Q.; Ji, J.; Zhang, Y. Implantable Zinc-Oxygen Battery for In Situ Electrical Stimulation-Promoted Neural Regeneration. *Adv. Mater.* **2023**, *35*, No. 2302997.
(25) Abdi, S.; Nasiri, M.; Mesbahi, A.; Khani, M. H. Investigation of Uranium (VI) Adsorption by Polypyrrole. *J. Hazard. Mater.* **2017**, *332*, 132−139.
(26) Seid, L.; Lakhdari, D.; Berkani, M.; Belgherbi, O.; Chouder, D.; Vasseghian, Y.; Lakhdari, N. High-Efficiency Electrochemical Degradation of Phenol In Aqueous Solutions Using Ni-PPy and Cu-PPy Composite Materials. *J. Hazard. Mater.* **2022**, *423*, No. 126986.
(27) Kim, D. H.; Lu, N.; Ma, R.; Kim, Y. S.; Kim, R. H.; Wang, S.; Wu, J.; Won, S. M.; Tao, H.; Islam, A.; Yu, K. J.; Kim, T. I.; Chowdhury, R.; Ying, M.; Xu, L.; Li, M.; Chung, H. J.; Keum, H.; McCormick, M.; Liu, P.; Zhang, Y. W.; Omenetto, F. G.; Huang, Y.; Coleman, T.; Rogers, J. A. Epidermal Electronics. *Science* **2011**, *333*, 838−843.
(28) Gillies, A. R.; Lieber, R. L. Structure and Function of the Skeletal Muscle Extracellular Matrix. *Muscle Nerve* **2011**, *44*, 318−331.
(29) Cangemi, G.; Reggiardo, G.; Barco, S.; Barbagallo, L.; Conte, M.; D'Angelo, P.; Bianchi, M.; Favre, C.; Galleni, B.; Melioli, G.; Haupt, R.; Garaventa, A.; Corrias, M. V. Prognostic Value of Ferritin, Neuron-Specific Enolase, Lactate Dehydrogenase, and Urinary and Plasmatic Catecholamine Metabolites in Children with Neuroblastoma. *Oncotargets Ther* **2012**, *5*, 417−423.
(30) Lionetto, L.; Lostia, A. M.; Stigliano, A.; Cardelli, P.; Simmaco, M. HPLC-Mass Spectrometry Method for Quantitative Detection of Neuroendocrine Tumor Markers: Vanillylmandelic Acid, Homovanillic Acid and 5-Hydroxyindoleacetic Acid. *Clin. Chim. Acta* **2008**, *398*, 53−56.
(31) Wang, J.; Zhao, L.; Yan, B. Postsynthetic Functionalization of Covalent Organic Frameworks for Dual Channel Fluorescence Diagnosis of Two Indicators Related to Parkinson's Disease. *Sensor Actuat B-Chem.* **2022**, *355*, No. 131297.
(32) Shetty, S. S.; El-Demellawi, J. K.; Khan, Y.; Hedhili, M. N.; Arul, P.; Mani, V.; Alshareef, H. N.; Salama, K. N. Iron Single-Atom Catalysts on MXenes for Ultrasensitive Monitoring of Adrenal Tumor Markers and Cellular Dopamine. *Adv. Mater. Technol.* **2023**, *8*, No. 2202069.
(33) Wu, X. D.; Zhao, P. F.; Tang, S. S.; Chen, Y.; Tang, K. L.; Lei, H. B.; Yang, Z. X.; Zhang, Z. H. Metal Organic Framework-Based


https://doi.org/10.1021/acsnano.3c11641
*ACS Nano* XXXX, XXX, XXX−XXX

Tricolor Fluorescence Imprinted Sensor for Rapid Intelligent Detection of Homovanillic Acid. *Microchem J.* **2023**, *190*, No. 108607.
(34) Wang, M.; Yang, Y.; Min, J.; Song, Y.; Tu, J.; Mukasa, D.; Ye, C.; Xu, C.; Heflin, N.; McCune, J. S.; Hsiai, T. K.; Li, Z.; Gao, W. A Wearable Electrochemical Biosensor for the Monitoring of Metabolites and Nutrients. *Nat. Biomed Eng.* **2022**, *6*, 1225−1235.
(35) Erdem, O.; Es, I.; Saylan, Y.; Atabay, M.; Gungen, M. A.; Olmez, K.; Denizli, A.; Inci, F. In Situ Synthesis and Dynamic Simulation of Molecularly Imprinted Polymeric Nanoparticles on a Micro-Reactor System. *Nat. Commun.* **2023**, *14*, 4840.
(36) Mukasa, D.; Wang, M.; Min, J.; Yang, Y.; Solomon, S. A.; Han, H.; Ye, C.; Gao, W. A Computationally Assisted Approach for Designing Wearable Biosensors toward Non-Invasive Personalized Molecular Analysis. *Adv. Mater.* **2023**, *35*, No. e2212161.
(37) Mintz Hemed, N.; Leal-Ortiz, S.; Zhao, E. T.; Melosh, N. A. On-Demand, Reversible, Ultrasensitive Polymer Membrane Based on Molecular Imprinting Polymer. *ACS Nano* **2023**, *17*, 5632−5643.
(38) Wang, L.; He, E.; Gao, R.; Wu, X. T.; Zhou, A. W.; Lu, J.; Zhao, T.; Li, J. X.; Yun, Y. J.; Li, L. H.; et al. Designing Porous Antifouling Interfaces for High-Power Implantable Biofuel Cell. *Adv. Funct. Mater.* **2021**, *31*, No. 2107160.
(39) Zhang, J.; Li, G.; Qu, Y.; Guo, Z.; Zhang, S.; Li, D. Fabrication and Hemocompatibility Evaluation of a Robust Honeycomb Nanostructure on Medical Pure Titanium Surface. *ACS Appl. Mater. Interfaces* **2022**, *14*, 9807−9823.
(40) Verschuur, C. V. M.; Suwijn, S. R.; Boel, J. A.; Post, B.; Bloem, B. R.; van Hilten, J. J.; van Laar, T.; Tissingh, G.; Munts, A. G.; Deuschl, G.; et al. Randomized Delayed-Start Trial of Levodopa in Parkinson's Disease. *N Engl J. Med.* **2019**, *380*, 315−324.
(41) Kurian, M. A.; Gissen, P.; Smith, M.; Heales, S., Jr; Clayton, P. T. The Monoamine Neurotransmitter Disorders: An Expanding Range of Neurological Syndromes. *Lancet Neurol* **2011**, *10*, 721−733.


https://doi.org/10.1021/acsnano.3c11641
*ACS Nano* XXXX, XXX, XXX−XXX